

Role of Crystallographic Textures on Failure Behavior in HSLA Grade-420 Steel During Cold Rolling

Mohammad Masoumi, Cleiton Carvalho Silva, Igor Anjos Lemos, Luis Flavio Gaspar Herculano, and Hamilton Ferreira Gomes de Abreu

(Submitted August 4, 2016; in revised form December 29, 2016; published online February 27, 2017)

The microstructural and textural evolution was analyzed during rolling at room temperature to obtain detailed information about the failure behavior in HSLA grade-420 steel. Electron backscatter diffraction measurements were carried out in both non-cracked and cracked areas after cold rolling to find a correlation between microstructural parameters (i.e., grain orientation, grain boundary characteristics and Taylor factor) and crack propagation. The results showed that the crack tended to propagate along grains oriented with {001} planes parallel to the normal direction with high Taylor factor value. The special boundaries associated with the {111}, {110} and {221} planes were indicated as crack resistance, while $\Sigma 5$, 13a and 17a, which related to the {001} planes, were crack-susceptible. Transgranular cracking was subjected within grains with high Taylor factor, while mismatch in Taylor factor between neighboring grains could provide an easy path for intergranular crack propagation.

Keywords grain boundary characteristics, grain orientation, Taylor factor

1. Introduction

High-strength low-alloy (HSLA) steels are developed to substitute the low-carbon steels in space equipment and facilities, pressure vessels, offshore oil drilling platforms, building construction, storage tanks and the automotive industry to meet requirements for higher strength materials (Ref 1-3). HSLA steels are a kind of low-carbon (with other alloying elements) steel, guaranteeing good weldability and low crack sensitivity coefficient. Moreover, the minor additions of alloying elements such as Nb, V, Ti and Mo increase the mechanical properties via various mechanisms such as grain refinement, solid solution strengthening, precipitation hardening and increasing dislocation density (Ref 4, 5).

Cold working of materials into the final change is known as the main failure source during manufacturing. Cold rolling leads to microstructural breakdown, increasing the amount of stored energy by producing high dislocation density and subjected anisotropy. It is generally believed that deformation occurs in slip systems along the close-packed planes and crystallographic directions. This means that some regions are heavily deformed, and the consequences have the higher level of the stored energy (Ref 6, 7). It is well known that the orientation of the grains obtained during manufacturing processing causes different resistances against deformation. Taylor

theory was established to predict the yield response of grains to the induced stress state, based on the family of active slip systems. Moreover, the activation of slip systems depends on the crystallographic orientation and local stress differences near grain boundaries between adjacent grains (Ref 8).

Excellent cold forming performance and high brittle fracture resistance at room temperature result in cost-effective manufacturing for many automotive applications. A detailed understanding of failure at the crystal structure scale helps to explain the fracture behavior and to propose some methods to prevent failures. A fraction of manufacturing and services results in fatalities, property damage, environmental damage and loss of customer confidence (Ref 9). Thus, extensive studies (Ref 10-12) have been conducted to understand the failure mechanism and reduce the failure susceptibility. This paper provides detailed information on failure analyses based on crystallographic texture and grain boundary distributions as a new approach to control failure damage. In this respect, microstructural and textural evolution was analyzed in as-received, solution heat-treated conditions, and two different regions of the cold sample (with and without cracks), to find a correlation between crystallographic orientations and failure behavior.

2. Experimental Procedures

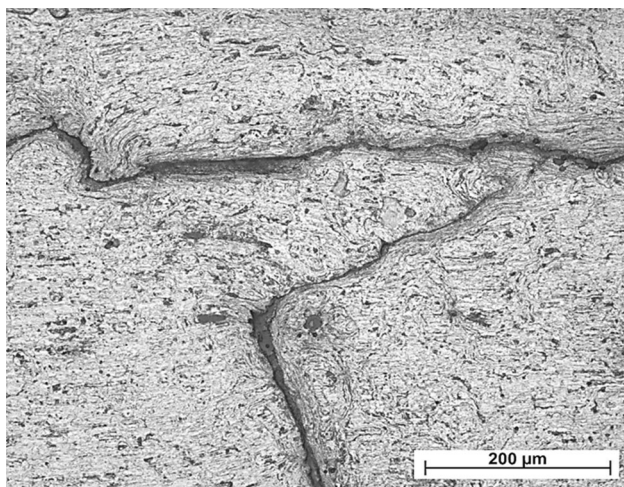
The initial material was a hot-rolled HSLA grade-420 strip of 8.5 mm thickness with a mean grain size of $8 \pm 1 \mu\text{m}$. The chemical composition of the alloy is listed in Table 1. Since phase boundaries and inclusions are preferred sites for micro-crack initiation, solution heat treatment at 1200 °C was conducted for 1 h as the first step for eliminating most of the inclusions to reduce the possibility of damage during rolling at room temperature.

Cold rolling was performed on a laboratory rolling mill with 100 mm roll radius, applying many passes at a low strain rate of 10^{-1} s^{-1} with less than 5% reduction per pass, up to crack occurrence at 95% total reduction (Fig. 1). The as-received, solution heat-treated, and cold-rolled samples

Mohammad Masoumi, Igor Anjos Lemos, Luis Flavio Gaspar Herculano, and Hamilton Ferreira Gomes de Abreu, Materials Characterization Laboratory, Department of Materials and Metallurgical Engineering, Building 729, Federal University of Ceará (UFC), Fortaleza, Ceará, Brazil; and Cleiton Carvalho Silva, Welding Engineering Laboratory, Department of Materials and Metallurgical Engineering, Building 715, Federal University of Ceará (UFC), Fortaleza, Ceará, Brazil. Contact e-mail: mohammad@alu.ufc.br.

Table 1 Chemical composition of material tested (mass fraction, %)

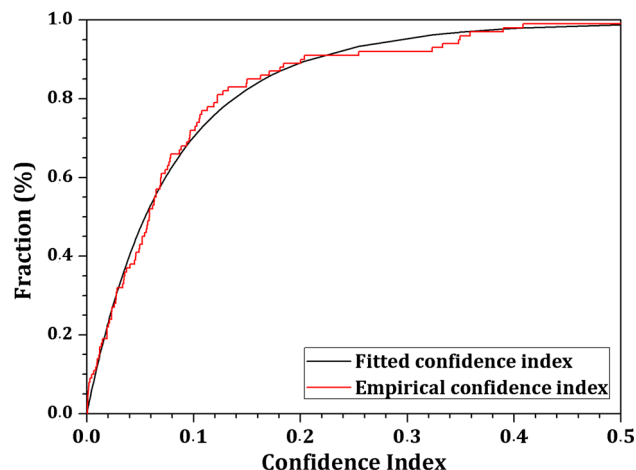
C	Si	Mn	S	Al	Cu	Cr	P	Ni	Mo	Nb	Ti	V
0.099	0.258	1.664	0.005	0.04	0.014	0.021	0.018	0.022	0.816	0.061	0.02	0.050

**Fig. 1** Crack appearance after cold rolling up to 95% reduction

were characterized using optical microscopy (OM, Olympus optical BX51 microscope), scanning electron microscopy (SEM, FEI Quanta FEG 450), x-ray diffraction (XRD, Phillips X-Pert) and Vickers hardness (Knoop Hardness Tester, QV-1000 Series) measurements. For metallographic analysis, standard grinding and polishing were carried out. Next, the samples were etched with 2% Nital solution to be analyzed with scanning electron microscopy. Furthermore, Vickers hardness was measured with a Shimadzu HMV hardness tester in the mentioned plane with 4.903 N indentation loads for 15 s (HV0.5). The average grain size was also measured by the diameter of the equivalent area with individual grains using Image-Pro software on an Olympus optical BX51 microscope.

Macrotextural measurements were carried out using a Phillips X-Pert diffractometer equipped with a texture goniometer. Three incomplete pole figures, i.e., {110}, {200} and {211} were obtained, using Cu radiation, in reflection mode on a 5° grid up to 85° sample tilt. Orientation distribution functions (ODFs) were calculated with the MTEX-free and open source software toolbox. The ODFs were presented in constant φ_2 sections under Euler notation system.

Electron backscatter diffraction (EBSD) analysis was conducted using the Channel 5 data processing software package (Oxford Instruments) installed on SEM (FEI Quanta FEG 450). The backscattered electrons generated from the sample as a result of primary electron-specimen interaction project a characteristic diffraction pattern (Kikuchi pattern) following Bragg's diffraction conditions. The principles of Kikuchi pattern generation and analysis were addressed in a review by Dingley and Randle (Ref 13). The working distance was set to about 13 mm with a tilt angle of 70°. The accelerating voltage of the gun was adjusted to 25 kV. Some deformed crystallographic structures produced Kikuchi patterns, of which the particular orientation is difficult to determine. Confidence Index (CI) is considered as an integral part of the indexing process,

**Fig. 2** Confidence index in cold-deformed sample obtained by EBSD measurement

providing a numerical measure of indexing quality (Ref 14) and is presented in Fig. 2 to show whether the EBSD results are reliable. The low confidence factor refers to low indexing patterns, while CI greater than 0.1 or 0.2 can achieve successfully indexing (Ref 15). Moreover, the point-to-point misorientation distribution was analyzed based on the assumption that the misorientation angles from 2° to 5° imply low-angle boundaries (LABs), while the misorientation angles between 5° and 15° are medium-angle boundaries (MABs), and greater than 15° are high-angle boundaries (HABs).

3. Results and Discussion

3.1 Microstructural Evolution

The SEM microstructure of the investigated samples is shown in Fig. 3. The as-received HSLA grade-420 steel with a banded ferrite-pearlite parallel to the rolling direction including quasi-polygonal ferrite, as a typical structure of hot rolling with partial recrystallisation during the forming process, is presented in Fig. 3(a). The average ferrite grain size and hardness were measured $8 \pm 1 \mu\text{m}$ and $165 \pm 5 \text{HV}$, respectively. According to Zener-Stroh (Ref 16, 17), dislocations glide along slip planes until they are stopped at phase boundaries. In other words, phase boundaries act as obstacles to slip and dislocation movement. This dislocation piles up, enhancing microcrack nucleation and facilitating crack propagation (Ref 18). Solution heat treatment at 1200 °C for 1 h followed by air cooling was carried out to break down the banded ferrite-pearlite to reduce the number of dislocation movement obstacles. Therefore, the solution heat-treated sample presents a polygonal ferrite, granular bainite and degenerated pearlite microstructure (Fig. 3b). The significant grain growth and hardness reduction resulted in solution treatment. The average grain size and

hardness were $13 \pm 1 \mu\text{m}$ and $195 \pm 5 \text{HV}$, respectively. The hardness increase can be explained by the phase transformations and increase in atomic distance due to the carbon occupation on octahedral positions in the cube lattice (Ref 19). Finally, a severely deformed microstructure was obtained by severe cold deformation (95% cold thickness reduction), presented in Fig. 3(c). Ferrite grain size reduced from 13 ± 1 to $2 \pm 1 \mu\text{m}$. The hardness was $318 \pm 7 \text{HV}$ because of the grain fragments, local stress concentrations and strain hardening governed by increasing the dislocation density.

3.2 Macrotextural Analysis

Crystallographic orientations were characterized by the XRD technique as an average method to characterize preferred orientation. In the cubic structure, the calculated ODFs from three incomplete pole figures (i.e., $\{110\}$, $\{200\}$ and $\{211\}$) are presented in four sections at $\varphi_2 = 0^\circ$, 25° , 45° and 65° . The calculated ODFs of the as-received sample in different sections are presented in Fig. 4. The predominant rotated cube $(001)\langle 110 \rangle$ textural components are identified in this sample. The deformed austenite grains produced by hot rolling during manufacturing processing are converted into equiaxed austenite grains with cubic $(001)\langle 010 \rangle$ orientation. Then, ferrite transformation during air cooling leads to the development of rotated cube components (Ref 20). Moreover, the presence of grains oriented in the $\{111\}$ and $\{110\}$ planes parallel to the rolling plane is common in this condition. Also, the dominant $\{111\}\langle 112 \rangle$ textural components can be attributed to the partial recrystallisation of austenite grains followed by ferrite trans-

formation (Ref 21). Furthermore, solution heat treatment followed by air cooling developed a significant $\{110\}\langle 1\bar{1}0 \rangle$ texture fiber, which was dominant of the Brass $(110)\langle 1\bar{1}2 \rangle$ to Goss $(110)\langle 001 \rangle$ components (Fig. 5). The development of the $(110)\langle 1\bar{1}8 \rangle$ component is clearly observed in sections at $\varphi_2 = 0^\circ$ and 45° . Recently, Kim et al. (Ref 22) studied the hot rolling process of an electrical steel. They showed that the Brass with a spread toward Goss crystallographic orientations were developed due to shear deformation during dynamic recrystallisation. Paul et al. (Ref 23) also reported that the shear transformation mechanism led to rotation around $\{110\}\langle 110 \rangle$ and the formation of Brass to Goss crystallographic orientations.

The crystallographic textural evolution after severe deformation is shown in Fig. 6. Higher textural intensity resulted in severe cold deformation, as expected. During cold rolling, shear strain was generated by the friction between the surface of the strip and the rolls. It is well documented (Ref 24, 25) that the pencil glides are the main factor responsible for the body-centered cubic (BCC) structure with low stacking fault energy (SFE), introducing shear deformation. The macrotextural analyses showed that the previous textural components were eliminated, and new orientation (such as $(001)\langle 120 \rangle$ and $(001)\langle \bar{1}\bar{1}0 \rangle$) textural components with high intensity were developed. Li et al. (Ref 26) reported that $(001)\langle 120 \rangle$ components formed by strain-induced boundary migration increased the local stress distribution uniformity during straining at room temperature. Moreover, the formation of grains strongly associated with $\{001\}$ planes parallel to normal direction suggests that the

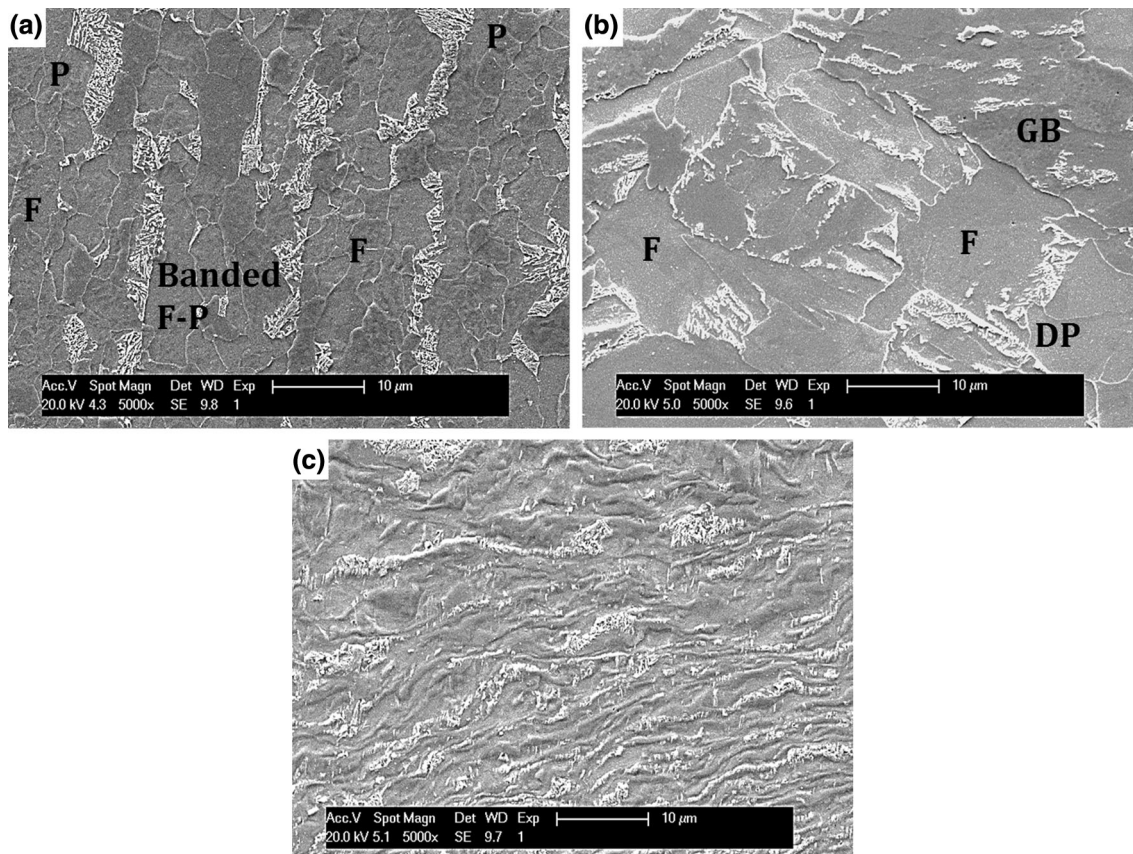


Fig. 3 SEM microstructure of the (a) as-received, (b) solution heat-treated and (c) cold-rolled samples (ferrite = F, pearlite = P, banded ferrite-pearlite = Banded F-P, granular bainite = GB, degenerated pearlite = DP)

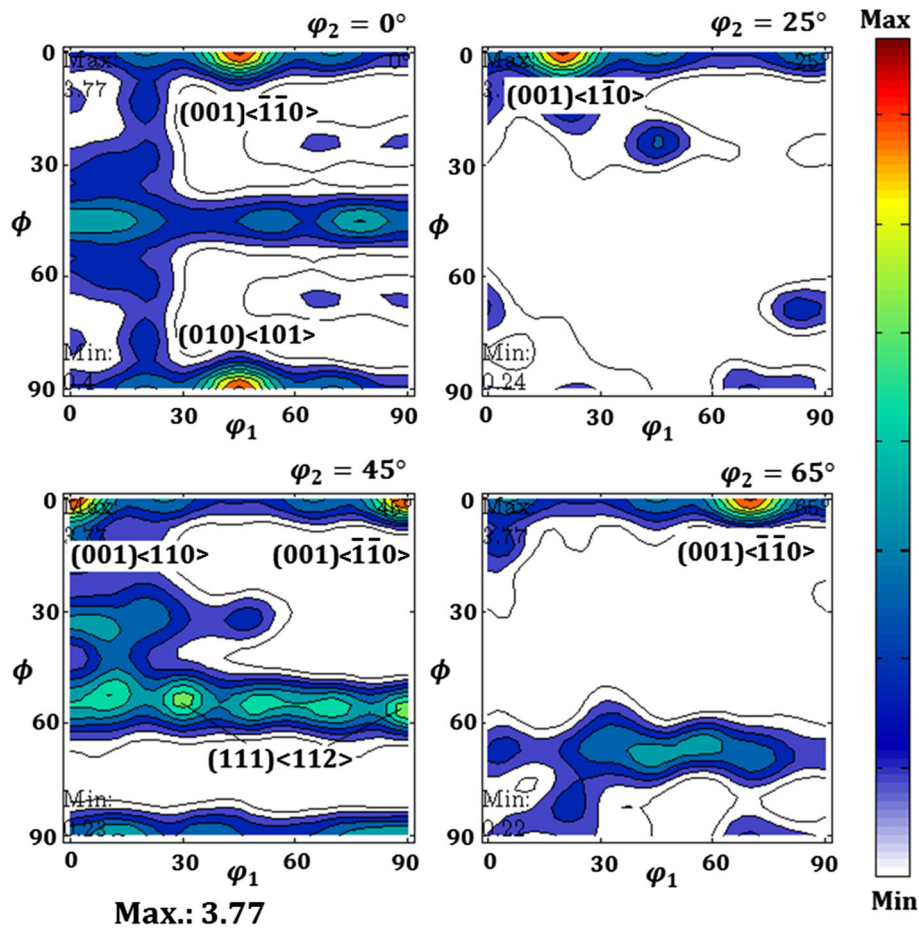


Fig. 4 ODFs at $\phi_2 = 0^\circ, 25^\circ, 45^\circ$ and 65° of as-received sample

deformation within this area obeyed plane-strain compression (Ref 22, 27). Kumar et al. (Ref 27) also identified that the $(001)\langle\bar{1}\bar{1}0\rangle$ of martensite phase texture component was formed by 50% cold deformation in low-carbon grade-304 stainless steel. This indicates that severe cold deformation caused the BCC martensite. Carbon cannot occupy the octahedral positions in the BCC lattice, resulting in the formation of BCC martensite instead of body-centered tetragonal (BCT) martensite (Ref 28).

3.3 Microtextural Evolution

In order to elucidate detailed information about the effect of crystallographic orientation and grain boundary characteristics on crack behavior, failure analysis was carried out using the EBSD technique. Figure 7(a) and (b) shows the normal direction inverse pole figure (IPF) maps in two different regions: non-cracked and cracked areas after cold rolling. The average confidence index obtained by EBSD was 70 and 50% in the non-cracked and cracked areas, respectively. Band contrast and band slope are the image quality factor derived from the average intensity of the Kikuchi bands concerning the overall intensity of the field of interest. The values are scaled to the range of 0–255 (i.e., low to high contrast). The distribution of the value of band contrast of each measurement is presented in Fig. 7(c), i.e., the higher the value, the sharper the image. Moreover, the invalid indexing solution (or zero solutions) is generated by very poor quality or defects such as grain

boundaries, cracks, dislocation clusters, voids, inclusions or areas around damage. The IPFs revealed that the cracks propagated along preferred grain orientations and/or grain boundaries. The plane-strain condition is considered by the rolling process. Thus, the surface is deformed plastically, while a compressive stress restrains crack growth in the surface layer. Cracks initiate around discontinuities and defects (such as inclusions and voids, or around pile-up dislocations) in the subsurface layers, where the compressive stress is lower. The cracks propagated horizontally in the shear band plane, leading to the breakdown of weaker regions.

The ODFs at different sections in the non-cracked and cracked regions after cold rolling were calculated from the related IPFs and are shown in Fig. 8. It is notable that the x-ray emitted by XRD penetrates up to 250 μm into the surface (in the shape of pear or water drop), providing an average estimation of the orientation in the whole sample. In contrast, textural analysis in the small specific region of definite grain numbers with the EBSD technique cannot give the crystallographic orientations of the entire sample (Ref 29). However, this method permits detailed information of the influence of grain orientation, boundary characteristics and local texture on the crack propagation path to be found.

The $(001)\langle 210\rangle$, $(001)\langle 2\bar{3}0\rangle$ components were identified in the non-cracked region. The dominant $(111)\langle 110\rangle$ components were also observed in the mentioned region. The rotated cube $(001)\langle 110\rangle$ and $(001)\langle 210\rangle$ textural components were characterized in a region close to the crack propagation path. The

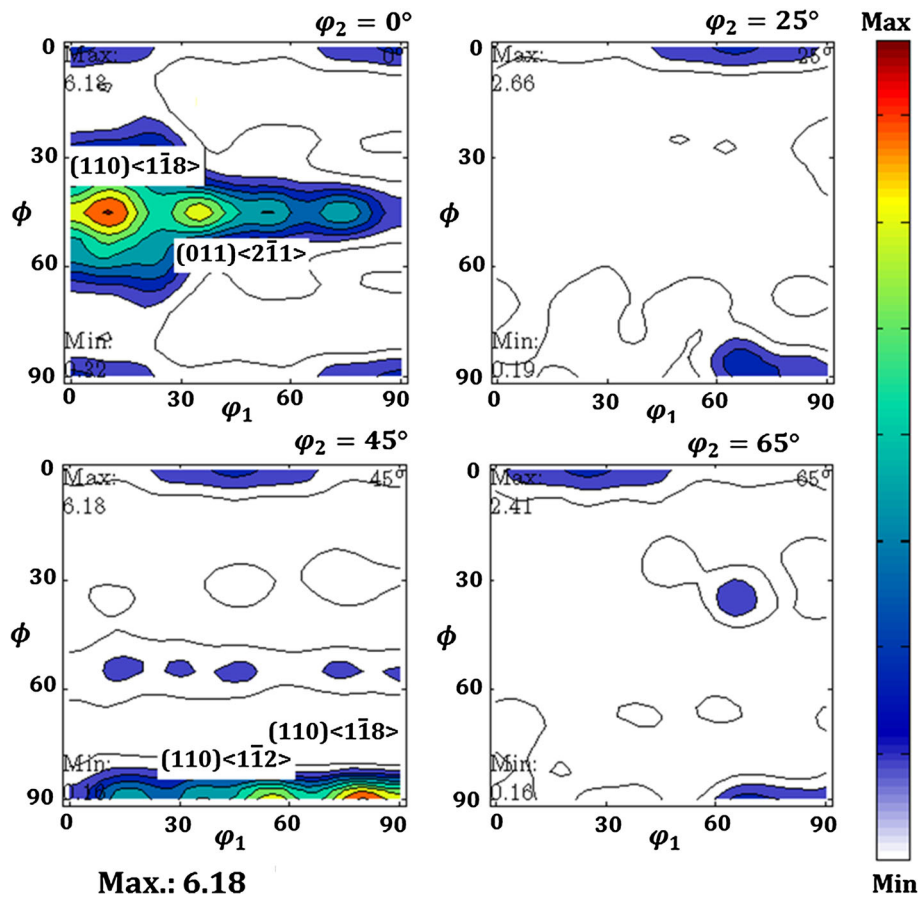


Fig. 5 ODFs at $\phi_2 = 0^\circ, 25^\circ, 45^\circ$ and 65° of solution heat-treated sample

(001) \langle 210 \rangle components are common for both the cracked and non-cracked regions. Conversely, the (111) \langle 110 \rangle crystallographic orientations developed in the non-cracked region. The development of $\{001\}$ //ND textural components indicated the dominant shear deformation during plain strain conditions. In-situ synchrotron x-ray diffraction analysis during tensile loading revealed that $\{001\}$ crystallographic planes accumulate much larger lattice strain compared to $\{111\}$ planes (Ref 30). This was because of the absence of sufficient slip systems due to the low dense packing of atoms and large distance between atoms in the BCC lattice. Also, the rotated cube component that is inclined at 45° to the rolling direction caused a large shear stress, leading to a significant reduction in mechanical resistance (Ref 31). In contrast, the non-cracked area had remarkable γ -fiber ($\{111\}$ //ND), which is considered as a favorable texture component to improve mechanical properties. Sugiura et al. (Ref 32) mentioned that selective boundary migration nuclei with (111) \langle 011 \rangle orientation into the (111) \langle 112 \rangle play a significant role in developing a rather homogenous deformation through the material. Thus, dislocation is not accumulated in these boundaries, leading to a retardation of microcrack nucleation.

3.4 Mesotextural Studies

The misorientation between two neighboring lattices is a major factor that contributes to the inducement of strain (Ref 33). Concerning the lattice distortion, a direct relationship was observed between the average boundary misorientation angle

and the strain induced, causing crack nucleation and propagation. The distribution of boundary types in both non-cracked and cracked regions was analyzed from IPFs and is shown in Fig. 9. It is well known that the lower stored energy is attributed to the lower misorientation between adjacent lattices. However, plausible failure is expected from higher stored energy due to the higher distortion in the neighboring grains. Rohrer et al. (Ref 34) showed that LABs with good atomic fit and the low level of incoherence between adjacent lattices act as obstacles against microcrack nucleation and propagation. Figure 9 shows that a higher volume fraction of LABs belongs to the non-cracked regions. In contrast, the cracked area demonstrated a remarkably higher amount of HABs. Therefore, the stored energy due to atomic misfit orientation enhances microcrack nucleation and facilitates crack propagation. The average boundary misorientation angle (θ_{ave}) was about 12.85° in the non-cracked region. This means that crystallographic orientations contributed to providing sufficient slip systems to facilitate dislocation gliding and to reduce local strain concentration. On the contrary, the average misorientation angle in region close to the crack path was $\theta_{ave} = 20.67^\circ$, showing the significant increase in lattice distortion and local strain concentration, leading to microcrack nucleation.

Special boundaries or coincidence site lattice (CSL) boundaries are also considered as obstacles against crack propagation, leading to an enhancement in the fracture toughness. The higher fraction of CSL boundaries that was found in non-cracked region is in agreement (Fig. 9). Moreover, the detailed information of the type of special boundaries in both regions is

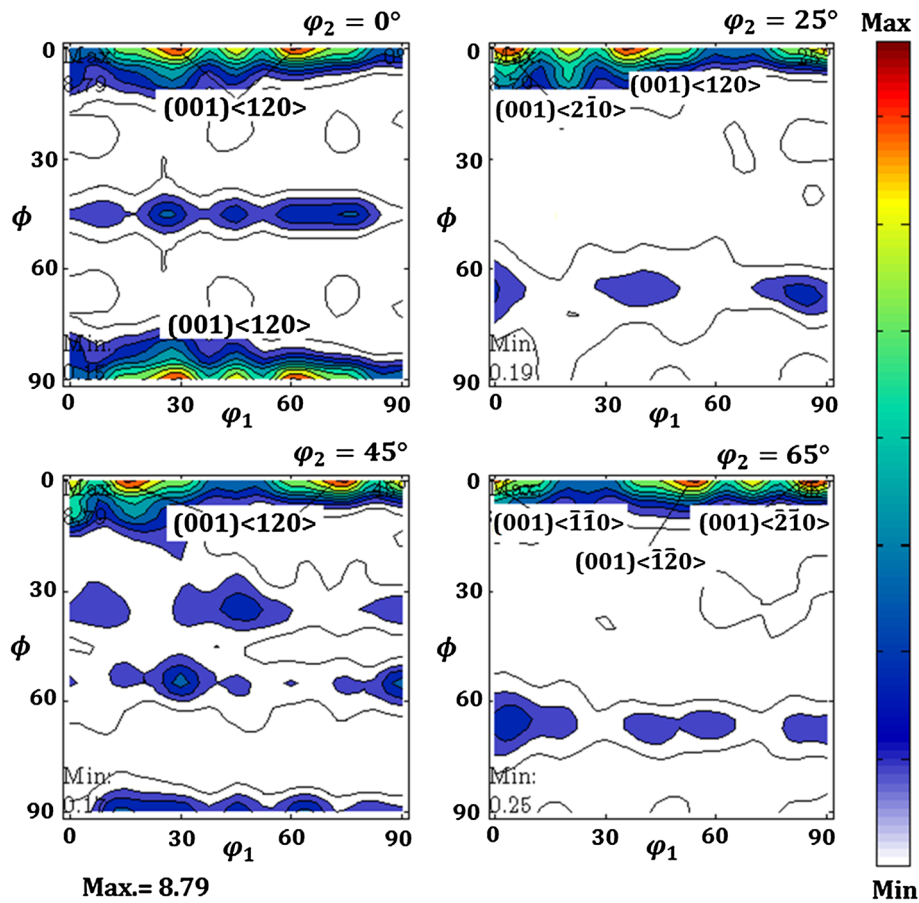


Fig. 6 ODFs at $\phi_2 = 0^\circ, 25^\circ, 45^\circ$ and 65° of cold-rolled sample

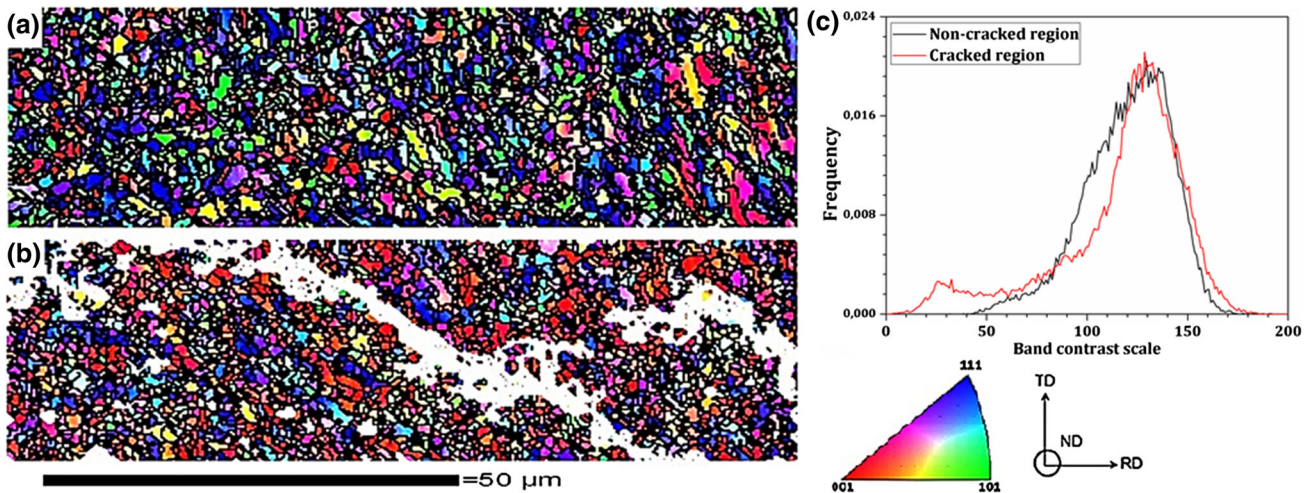


Fig. 7 Normal direction IPFs in (a) non-cracked, (b) cracked regions and (c) distribution of band contrast

presented in Fig. 10. As mentioned earlier, the orientation corresponded to the close-packed planes in BCC such as $\{110\}$, $\{111\}$ and $\{112\}$ acts as crack resistance, while the $\{001\}$ as the lowest dense plane with the highest stored energy is crack-susceptible. It was observed that special boundaries composed mainly $\Sigma 3, 9, 11, 13b$ and $17b$ that are related to $\{111\}$, $\{110\}$ and $\{221\}$ planes had higher frequency in the non-cracked area. In contrast, $\Sigma 5, 13a$ and $17a$ associated with $\{001\}$ planes

were dominant in the cracked area. As a result, it is worth mentioning that the boundary planes associated with $\{001\}$ known with the lowest dense plane in the BCC lattice are more susceptible to inducing deformation and failure, while the boundary planes related to $\{110\}$ and $\{111\}$ corresponded to dense planes, and preferred slip direction enhancing dislocation gliding to prevent dislocation accumulation and to increase fracture resistance.

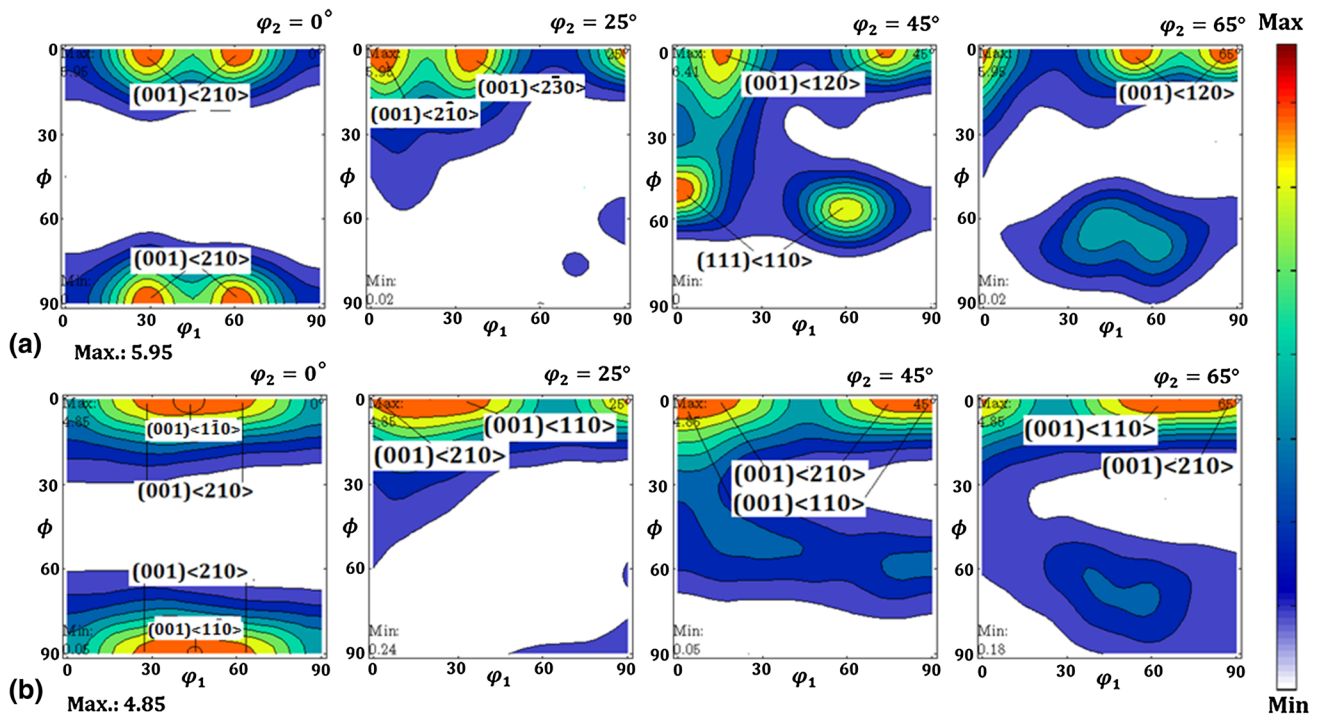


Fig. 8 Calculated ODFs at $\phi_2 = 0^\circ, 25^\circ, 45^\circ$ and 65° sections obtained from IPFs of (a) non-cracked and (b) cracked regions after cold rolling

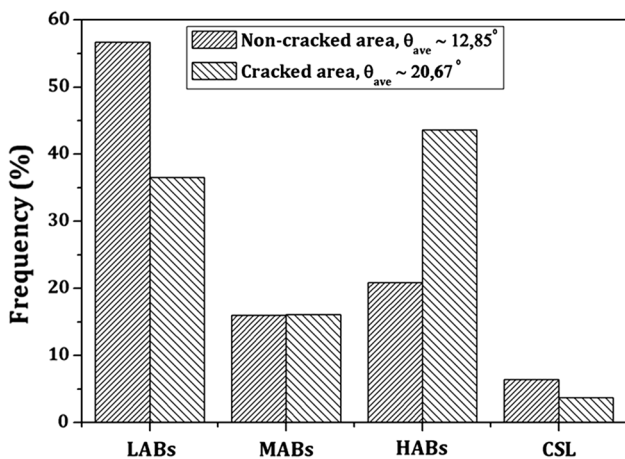


Fig. 9 Distribution of boundary types in both non-cracked and cracked regions

In order to find a correlation between grain orientation and deformation tendency of grains, Taylor factor analysis was carried out. Taylor's theory supposed that the critical resolved shear stress on all the active slip systems is the same. Regarding the Von Mises criterion, at least five slip systems are required for plastic deformation (Ref 35, 36). Thus, Taylor estimates the expenditure energy for all possible sets of slip systems consumed during deformation and the direction of applied stress. Then, the Taylor factor is assigned, which is related to the minimum energy of slip systems. In this respect, the crystals are categorized into three different groups. First, the crystals are already aligned with slip systems; thus, the minimum expenditure energy is required to meet plastic deformation (the lowest Taylor Factor). For the next group, the crystals would be rotated

in an arbitrary direction to accommodate appropriate slip plane positions where plastic deformation could take place. In the final group, crystals are not able to rotate and provide appropriate slip planes, called hard grains, and are thus highly prone to crack formation and breakdown. Figure 11 shows the IPF, Taylor factor map and distribution of Taylor factor for the cracked region.

The OIM (orientation imaging microscopy) results obtained from a relatively high number of grains in the vicinity of a crack are shown in Fig. 11. High dislocation density grains surrounding the crack are observed in the IPF map. Thus, these grains have high stored energy with high Taylor factor, leading to high resistance against deformation. The high Taylor factor grains require larger stress to accommodate sufficient slip systems for deformation. Higher stress generates more dislocations, leading to inhomogeneity in the grain interior and in the regions close to the grain boundaries. Crystallographic orientation distributions around the vicinity of the crack demonstrate that the crack tended to propagate along grains oriented with the $\{001\}$ orientation. Moreover, cracks favorably propagated along grains with high Taylor factor, which exhibited less resistance against crack propagation. The grains in dark yellow (Fig. 11b) were orientated for relatively hard slip and tended to be resistant to deformation. Thus, it is likely to form intergranular cracking, while gains in light red with high Taylor factor were subjected to transgranular cracking. Moreover, the mismatch in Taylor factor between neighboring grains could provide an easy path to intergranular crack propagation. The most important point here is that the crack would propagate along grains oriented with $\{100\}$ planes parallel to the normal direction, and the high Taylor factor could facilitate the crack growth. These findings are also in good agreement with our previous results, which demonstrated that $\{100\}$ //ND grains are susceptible to crack initiation and propagation.

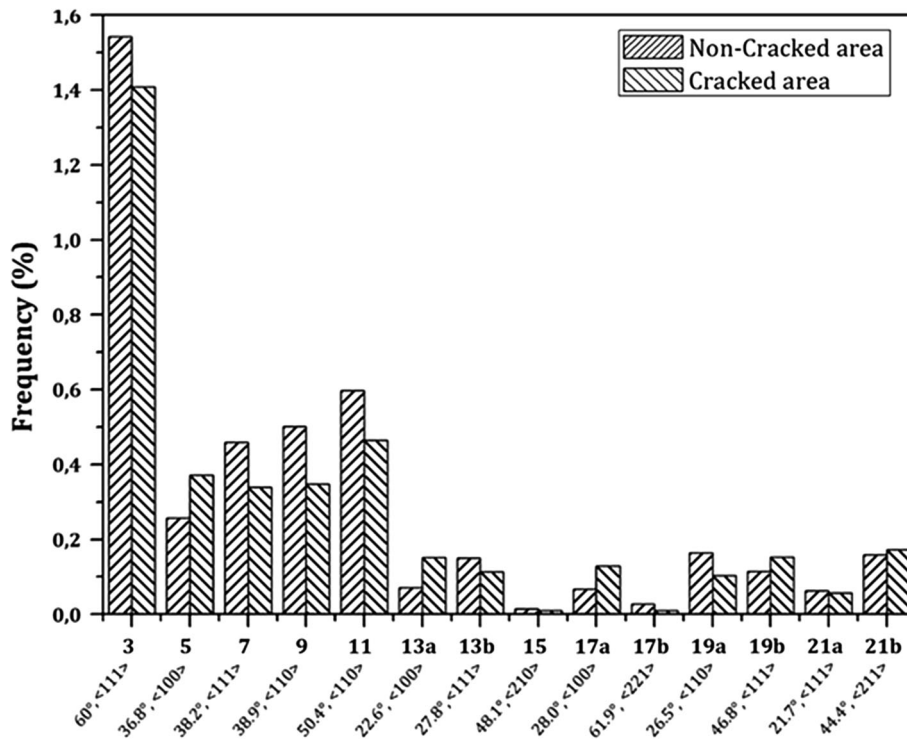


Fig. 10 Detailed information of special boundary distributions

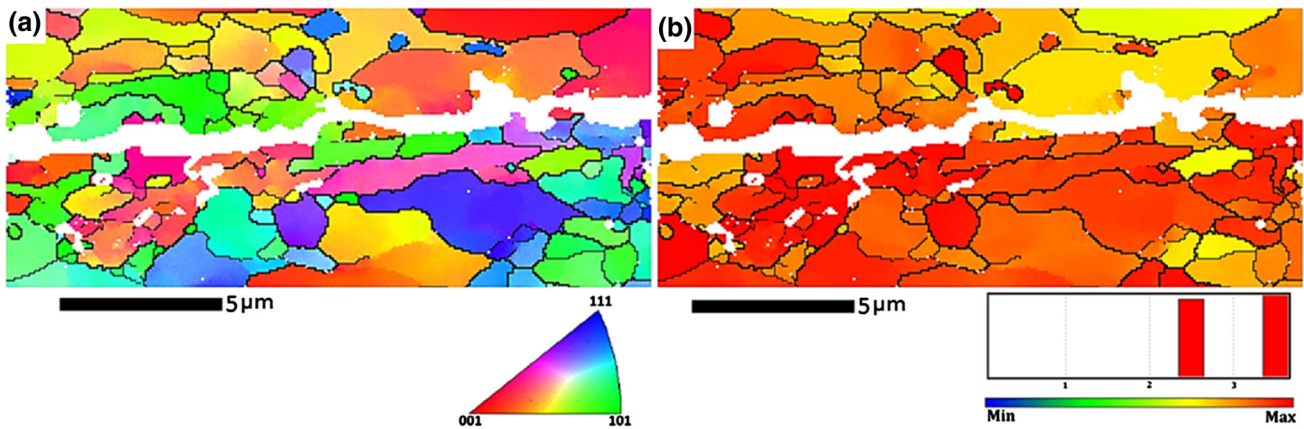


Fig. 11 (a) IPF map, (b) Taylor factor map for the cracked region

4. Conclusions

The evolution of the microstructure, and macro- and micro-texture during cold rolling in HSLA grade-420 steel was investigated to obtain detailed information about failure behavior. Then, the EBSD technique was used to find a correlation between microstructural parameters (i.e., grain orientation, grain boundary characteristics and Taylor factor) and crack propagation. The main conclusions of the study are as follows:

- The cracked appearance at the surface was attributed to the relatively large amount of shear strain imposed by the rolls and strip.
- The presence of a high number of grains oriented $\{001\}$ parallel to the normal direction makes the

sample highly susceptible to crack nucleation and propagation.

- Cracks tend to propagate along high-angle grain boundaries associated with grains with high Taylor factor values.
- The $(001)\langle 110 \rangle$ component was prone to crack propagation, while the $(001)\langle 120 \rangle$ and $(111)\langle 110 \rangle$ components were highly resistant against crack propagation.
- The special boundaries associated with the $\{111\}$, $\{110\}$ and $\{221\}$ planes were indicated as crack resistance, while $\Sigma 5$, 13a and 17a, which related to the $\{001\}$ planes, were crack-susceptible.
- Transgranular cracking was subjected within grains with high Taylor factor, while the mismatch in Taylor factor between neighboring grains could provide an easy path for intergranular crack propagation.

Acknowledgments

The authors acknowledge the CNPq and CAPES for financial support and the research board of the Universidade Federal do Ceará, Laboratório de Caracterização de Materiais (LACAM) and Central Analítica-UFC/CT-INFRA/MCTI-SISNANO/Pró-Equipamentos for providing the research facilities of this work.

References

1. S.R. Nathan, V. Balasubramanian, S. Malarvizhi, and A.G. Rao, Effect of Welding Processes on Mechanical and Microstructural Characteristics of High Strength Low Alloy Naval Grade Steel Joints, *Def. Technol.*, 2015, **11**, p 308–317
2. S.R. Nathan, S. Malarvizhi, V. Balasubramanian, and A.G. Rao, Failure Analysis of Tungsten Based Tool Materials Used in Friction Stir Welding of High Strength Low Alloy Steels, *Eng. Fail. Anal.*, 2016, **66**, p 88–98
3. S. Ravi, V. Balasubramanian, and S.N. Nasser, Effect of Mismatch Ratio (MMR) on Fatigue Crack Growth Behaviour of HSLA Steel Welds, *Eng. Fail. Anal.*, 2004, **11**, p 413–428
4. L. Falat, L. Čiripová, J. Kepič, J. Buršík, and I. Podstranská, Correlation Between Microstructure and Creep Performance of Martensitic/Austenitic Transition Weldment in Dependence of Its Post-weld Heat Treatment, *Eng. Fail. Anal.*, 2014, **40**, p 141–152
5. L. Zhongqiu, F. Jian, Z. Yong, and Y. Zexi, Influence of Quenching On-Line on Properties of X70 Steel for Sour Service Seamless Pipe, *Energy Procedia*, 2012, **16**, p 444–450
6. Y. He and E.J. Hilinski, Texture and Magnetic Properties of Non-oriented Electrical Steels Processed by an Unconventional Cold Rolling Scheme, *J. Magn. Magn. Mater.*, 2015, **405**, p 337–352
7. T. Liebe, A. Menzel, and P. Steinmann, Theory and Numerics of Geometrically Non-linear Gradient Plasticity, *Int. J. Eng. Sci.*, 2003, **41**, p 1603–1629
8. K.J. Kurzydowski, R.A. Varin, and W. Zielinski, In Situ Investigation of the Early Stages of Plastic Deformation in an Austenitic Stainless Steel, *Acta Metall.*, 1984, **32**, p 71–78
9. A.K. Jha, S.K. Manwatkar, P.R. Narayanan, B. Pant, S.C. Sharma, and K.M. George, Failure Analysis of a High Strength Low Alloy 0.15C-1.25Cr-1Mo-0.25 V Steel Pressure Vessel, *Eng. Fail. Anal.*, 2013, **4**, p 265–272
10. C.M. Lin, H.L. Tsai, C.D. Cheng, and C. Yang, Effect of Repeated Weld-Repairs on Microstructure, Texture, Impact Properties and Corrosion Properties of AISI, 304L Stainless Steel, *Eng. Fail. Anal.*, 2012, **21**, p 9–20
11. C.R. Gagg and P.R. Lewis, Wear as a Product Failure Mechanism—Overview and Case Studies, *Eng. Fail. Anal.*, 2007, **14**, p 1618–1640
12. B. Suyitno, T.D. Arifvianto, M. Widodo, P. Mahardika, and U.A. Dewo, Salim, Effect of Cold Working and Sandblasting on the Microhardness, Tensile Strength and Corrosion Resistance of AISI, 316L Stainless Steel, *JOM*, 2012, **19**, p 1093–1099
13. D.J. Dingley, K.Z. Baba-Kishi, and V. Randle, *Atlas of Backscattering Kikuchi Diffraction Patterns. Microscopy in Materials Science Series*, Institute of Physics Publishing, Philadelphia, 1995
14. D.P. Field, Recent Advances in the Application of Orientation Imaging, *Ultramicroscopy*, 1997, **67**, p 1–9
15. M.M. Nowell and S.I. Wright, Orientation Effects on Indexing of Electron Backscatter Diffraction Patterns, *Ultramicroscopy*, 2005, **103**, p 41–58
16. C. Zener, The Micro-mechanism of Fracture, *Fracturing of Metals*, American Society of Metals, Cleveland, 1948, p 3–31
17. A.N. Stroh, The Formation of Cracks as a Result of Pastic Flow, I, *Proc. R. Soc. Lond.*, 1954, **A223**, p 404–414
18. J. Jiang, J. Yang, T. Zhang, J. Zou, Y. Wang, F.P.E. Dunne, and T.B. Britton, Microstructurally Sensitive Crack Nucleation Around Inclusions in Powder Metallurgy Nickel-Based Superalloys, *Acta Mater.*, 2016, **117**(15), p 333–344
19. N.N. Rammo and O.G. Abdulah, A Model for the Prediction of Lattice Parameters of Iron-Carbon Austenite and Martensite, *J. Alloys Compd.*, 2006, **420**, p 117–120
20. J.J. Jonas, Transformation Textures Associated with Steel Processing, *Microstructure and Texture in Steels*, A. Haldar, S. Suwas, D. Bhattacharjee, Ed., Springer, London, 2009, p 3–17
21. S. Das, M. Mukherjee, and T.K. Pal, Effect of Grain Boundary Precipitation and δ -Ferrite Formation on Surface Defect of Low Nickel Austenitic Stainless Steels, *Eng. Fail. Anal.*, 2015, **54**, p 90–102
22. J.K. Kim, D.N. Lee, and Y.M. Koo, The Evolution of the Goss and Cube Textures in Electrical Steel, *Mater. Lett.*, 2014, **122**, p 110–113
23. H.A. Paul, A. Morawiec, E. Bouzy, and J.J. Fundenberger, Shear Banding in Twinned Structure of Copper Deformed at 77 K, *J. Microsc.*, 2006, **223**, p 256–259
24. F.J. Humphreys and M. Hatherly, *Recrystallization and Related Annealing Phenomena*, 2nd ed., Elsevier, Amsterdam, 2004, p 38–42
25. Sugondo, J.A. Szpunar, and P. Gangli, Development of Texture in Low-Carbon Steels for Cold Heading, *J. Mater. Process. Technol.*, 1991, **26**, p 305–321
26. H.Z. Li, H.T. Liu, Z.Y. Liu, and G.D. Wang, Microstructure, Texture Evolution and Magnetic Properties of Strip-Casting Non-oriented 6.5 wt% Si Electrical Steel Doped with Cerium, *Mater. Charact.*, 2015, **103**, p 101–106
27. B.R. Kumar, A.K. Singh, S. Das, and D.K. Bhattacharya, Cold Rolling Texture in AISI, 304 Stainless Steel, *Mater. Sci. Eng. A*, 2004, **364**(1–2), p 132–139
28. U.K. Viswanathan, G.K. Dey, and M.K. Asundi, Precipitation Hardening in 350 Grade Maraging Steel, *Metall. Trans. A*, 1993, **24**(11), p 2429–2442
29. A.J. Schwartz and M. Kumar, Ed., *Electron Backscatter Diffraction in Materials Science*, Kluwer Academic/Plenum Publishers, New York, 2000
30. D.M. Collins, M. Mostafavi, R.E. Todd, T. Connolly, and A.J. Wilkinson, A Synchrotron X-ray Diffraction Study of In Situ Biaxial Deformation, *Acta Mater.*, 2015, **90**, p 46–58
31. O. Engler, M.Y. Huh, and C.N. Tome, A Study of Through-Thickness Texture Gradients in Rolled Sheets, *Metall. Mater. Trans. A*, 2000, **31A**, p 2299
32. N. Sugiura, N. Yoshinaga, and K. Ushioda, Deformation Behavior of Electro-Deposited Pure Fe and Its Texture Evolution During Cold-Rolling and Subsequent Annealing, *Mater. Sci. Eng.*, 2015, **82**, p 120–153
33. J.A. Nucci, R.R. Keller, D.P. Field, and Y. Shacham-Diamand, Grain Boundary Misorientation Angles and Stress-Induced Voiding in Oxide Passivated Copper Interconnects, *Appl. Phys. Lett.*, 1997, **70**, p 1242
34. G.S. Rohrer, J. Gruber, and A.D. Rollett, A Model for the Origin of Anisotropic Grain Boundary Character Distributions in Polycrystalline Materials, *Appl. Texture Anal.*, 2008, **201**, p 710–714
35. M. Sachtleber, Z. Zhao, and D. Raabe, Experimental Investigation of Plastic Grain Interaction, *Mater. Sci. Eng. A*, 2002, **336**, p 81–87
36. D.N. Lee, Strain Energy Release Maximization Model for Evolution of Recrystallization Textures, *Int. J. Mech. Sci.*, 2000, **42**, p 1645–1678